Abnormal cardiac inflow patterns during postnatal development in a mouse model of Holt-Oram syndrome

Yu-Qing Zhou, Yonghong Zhu, Jonathan Bishop, Lorinda Davidson, R. Mark Henkelman, Benoit G. Bruneau and F. Stuart Foster

AJP - Heart 289:992-1001, 2005. First published Apr 22, 2005; doi:10.1152/ajpheart.00027.2005

AJP - Heart and Circulatory Physiology publishes original investigations on the physiology of the heart, blood vessels, and lymphatics, including experimental and theoretical studies of cardiovascular function at all levels of organization ranging from the intact animal to the cellular, subcellular, and molecular levels. It is published 12 times a year (monthly) by the American Physiological Society, 9650 Rockville Pike, Bethesda MD 20814-3991. Copyright © 2005 by the American Physiological Society. ISSN: 0363-6135, ESSN: 1522-1539. Visit our website at http://www.the-aps.org/.

Am J Physiol Heart Circ Physiol 289: H992–H1001, 2005.
First published April 22, 2005; doi:10.1152/ajpheart.00027.2005.

Abnormal cardiac inflow patterns during postnatal development in a mouse model of Holt-Oram syndrome

Yu-Qing Zhou,[1] Yonghong Zhu,[2,3] Jonathan Bishop,[1] Lorinda Davidson,[1] R. Mark Henkelman,[1,4,5] Benoit G. Bruneau,[2,3,6] and F. Stuart Foster[1,4,5]

[1]*Mouse Imaging Centre and* [2]*Cardiovascular Research Program, Hospital for Sick Children,* [3]*Heart and Stroke/Richard Lewer Centre of Excellence,* [4]*Sunnybrook and Women's College Health Sciences Centre,* [5]*Department of Medical Biophysics, and* [6]*Department of Molecular and Medical Genetics, University of Toronto, Toronto, Ontario, Canada*

Submitted 11 January 2005; accepted in final form 21 April 2005

Zhou, Yu-Qing, Yonghong Zhu, Jonathan Bishop, Lorinda Davidson, R. Mark Henkelman, Benoit G. Bruneau, and F. Stuart Foster. Abnormal cardiac inflow patterns during postnatal development in a mouse model of Holt-Oram syndrome. *Am J Physiol Heart Circ Physiol* 289: H992–H1001, 2005. First published April 22, 2005; doi:10.1152/ajpheart.00027.2005.—*Tbx5*$^{del/+}$ mice provide a model of human Holt-Oram syndrome. In this study, the cardiac functional phenotypes of this mouse model were investigated with 30-MHz ultrasound by comparing 12 *Tbx5*$^{del/+}$ mice with 12 wild-type littermates at 1, 2, 4, and 8 wk of age. Cardiac dimensions were measured with two-dimensional and M-mode imaging. The flow patterns in the left and right ventricular inflow channels were evaluated with Doppler flow sampling. Compared with wild-type littermates, *Tbx5*$^{del/+}$ mice showed significant changes in the mitral flow pattern, including decreased peak velocity of the left ventricular (LV) early filling wave (E wave), increased peak velocity of the late filling wave (A wave), and decreased or even reversed peak E-to-A ratio. The prolongation of LV isovolumic relaxation time was detected in *Tbx5*$^{del/+}$ neonates as early as 1 wk of age. In *Tbx5*$^{del/+}$ mice, LV wall thickness appeared normal but LV chamber dimension was significantly reduced. LV systolic function did not differ from that in wild-type littermates. In contrast, the Doppler flow spectrum in the enlarged tricuspid orifice of *Tbx5*$^{del/+}$ mice demonstrated increased peak velocities of both E and A waves and increased total time-velocity integral but unchanged peak E/A. In another 13 mice (7 *Tbx5*$^{del/+}$, 6 wild-type) at 2 wk of age, significant correlation was found between *Tbx5* gene expression level in ventricular myocardium and LV filling parameters. In conclusion, the LV diastolic function of *Tbx5*$^{del/+}$ mice is significantly deteriorated, whereas the systolic function remains normal.

Tbx5 mutation; atrial septal defect; left ventricular diastolic function; right ventricular dilatation; Doppler flow sampling

HUMAN HOLT-ORAM SYNDROME is an autosomal dominant disease caused by mutations of the *TBX5* gene and is characterized by congenital cardiac and forelimb anomalies (1, 4, 15, 16, 22). Similar to Holt-Oram syndrome, *Tbx5*$^{del/+}$ mice demonstrate cardiac anatomic abnormalities including atrial septal defects (ASDs) and/or ventricular septal defects and limb malformations. Secondary changes in cardiac morphology including dilated atria and right ventricle leading to a bulbous shape of the whole heart are observed. Abnormal cardiac electrophysiology, particularly atrioventricular block, has also been found (5, 23).

Although the cardiac structural phenotypes of *Tbx5*$^{del/+}$ mice have been well identified ex vivo with histology or MRI, the in vivo cardiac functional phenotypes and their comparison with those of corresponding human cardiac disease have not yet been evaluated. As seen in humans with right ventricular volume and/or pressure overload caused by ASD, left ventricular diastolic filling is impaired because of right heart dilatation and abnormal interaction of both ventricles (3, 6, 19, 30). Because ASD and resultant right heart dilatation are the major structural anomalies in *Tbx5*$^{del/+}$ mice, it is of interest to explore the consequent functional abnormalities of this model compared with those in humans. Another question is whether *Tbx5* mutation that markedly decreases the expression of downstream targeted genes in the developing murine heart (5) affects ventricular myocardial function.

Recently, a methodology has been established for comprehensive in vivo cardiac imaging in mice using a high-frequency (~20–55 MHz) ultrasound imaging, ultrasound biomicroscopy (UBM) (10–12, 25, 38, 40). This new technology has been successfully applied to measure cardiac dimensions, function, and hemodynamics with various functional modalities including two-dimensional (B mode) and M-mode imaging and Doppler flow sampling. One of the important applications in mouse cardiac functional phenotyping is to observe ventricular inflow patterns for evaluation of the diastolic function of the left and right ventricles.

This study was conducted to extensively evaluate the cardiac functional phenotypes of *Tbx5*$^{del/+}$ mice in vivo, with an emphasis on the ventricular diastolic function of both sides of the heart. Cardiac morphology, dimensions, ventricular systolic function, and Doppler flow patterns in cardiac inflow channels were noninvasively observed with UBM at 30 MHz in *Tbx5*$^{del/+}$ mice and compared with those of wild-type littermates during postnatal development from 1 to 8 wk.

MATERIALS AND METHODS

The experimental protocol for this study was approved by the Animal Care Committee of the Hospital for Sick Children, and the study was conducted in accordance with the guidelines established by the Canadian Council on Animal Care.

Mice

Group I. Tbx5$^{del/+}$ mice (5) were intercrossed with wild-type Black Swiss mice (Taconic Farms) for the next generation of mice. From three litters, 12 *Tbx5*$^{del/+}$ mice (8 males, 4 females) and 12 wild-type littermates (8 males, 4 females) were observed at 1, 2, 4, and 8 wk of age. Each mouse was coded and followed.

Address for reprint requests and other correspondence: Y.-Q. Zhou, Mouse Imaging Centre, Hospital for Sick Children, 555 University Ave., Toronto, ON, Canada M5G 1X8 (E-mail: yqzhou@sickkids.ca).

The costs of publication of this article were defrayed in part by the payment of page charges. The article must therefore be hereby marked "*advertisement*" in accordance with 18 U.S.C. Section 1734 solely to indicate this fact.

Group II. An additional 13 mice from two litters (7 *Tbx5*$^{del/+}$, 6 wild type) were studied at 2 wk of age to quantify *Tbx5* gene expression in the ventricular myocardium, which was then correlated with the ultrasound findings.

In Vivo Transthoracic Cardiac Imaging With UBM

A Vevo 660 UBM (VisualSonics, Toronto, ON, Canada) was used. It had a single-element mechanical transducer with a center frequency of 30 MHz and a frame rate of 30 Hz. The spatial resolution of B-mode imaging was ~115 μm (lateral) by ~55 μm (axial). Anesthesia of mice with isoflurane was induced at a concentration of 5% and then maintained at 1.5% by face mask. Mouse body temperature was monitored by rectal thermometer and maintained between ~36 and 38°C. The resultant heart rate is given in Table 1. Other details of technical specifications, animal preparations, and experimental procedures were described previously (38).

In each mouse, cardiac imaging was initiated in the apical four-chamber view to record the mitral and tricuspid Doppler flow spectra. The Doppler sample volume was placed at the center of the orifice and at the tip level of the valves for the highest velocities (Fig. 1*A*). However, for measurement of the left ventricular systolic and diastolic time intervals, the Doppler sample volume was moved slightly toward the left ventricular outflow tract to intersect with both the mitral inflow and the left ventricular outflow in the same recording.

The transducer was moved to the upper left parasternal region for visualization of the left ventricular outflow tract in its longitudinal axis, as well as the right atrium and right ventricle in the far field of the image (Fig. 1*C*). As suggested in our previous study (38), this specific imaging section was standardized to measure the dimensions of the right atrium and ventricle, which are irregularly shaped. In consideration of the relatively low frame rate of B-mode imaging, a cine loop with ~50 consecutive frames of images was recorded and 5 frames with the largest chamber dimensions during diastole (when the tricuspid valves were open) were selected for the measurements.

The transducer was moved down along the left parasternal window and tilted leftward to visualize the left ventricular inflow tract including the pulmonary vein, left atrium, mitral orifice, and left ventricle. Pulmonary venous flow was sampled just at the entrance of the right pulmonary vein to the left atrium. In the precordial region, M-mode recording of the left ventricle was made in both the long-axis and the short-axis sections at the tip level of the papillary muscles. A transversal section at the level of the heart base was then applied to visualize the main pulmonary artery. B-mode imaging was used to measure the diameter because it was difficult to make the M-mode cursor line perpendicular to the main pulmonary trunk. Five frames with the largest lumens during systole (when the pulmonary valves were open) were selected from a cine loop of ~50 consecutive frames for diameter measurements. Finally, from the right parasternal window, the right superior vena caval flow spectrum was sampled at its entrance to the right atrium. The complete examination for each mouse lasted ~30 min.

All UBM measurements were made according to the standards established in human echocardiography (27–29). In B-mode images, the width of the tricuspid ring was measured from the point where the interventricular septum attached to the right posterior wall of the aortic root to the junction of the right atrial and ventricular walls (Fig. 2, *A* and *B*). The moving tricuspid valves in real-time imaging helped to confirm the location of the tricuspid orifice. M-mode recordings of the left ventricle were analyzed for wall thicknesses and chamber dimensions. Fractional shortening was calculated as a measure of left ventricular systolic function (7). Three cardiac cycles were analyzed in each of the two sections, and then six sets of values were averaged.

From the mitral and tricuspid Doppler flow spectra, the peak velocities of the early ventricular filling wave (E wave), the late ventricular filling wave caused by atrial contraction (A wave), and the total time-velocity integral (TVI) of both E and A waves were measured. The left ventricular systolic and diastolic time intervals were measured from the mitral flow waveforms, as suggested by human studies (9, 20, 33). The isovolumic relaxation time (IVRT) was measured from the closure point of the aortic valves to the start of mitral flow. The ventricular diastolic filling time (DT) was from the start to the end of the mitral flow. The isovolumic contraction time (IVCT) was from the closure point of the mitral valve to the start of the aortic flow. The ventricular ejection time (ET) was from the start to the end of the aortic flow (Fig. 3*A*). All Doppler parameters were averaged for three consecutive cardiac cycles.

In analysis of the Doppler flow spectra from the pulmonary vein and right superior vena cava, the waveforms were first identified according to the simultaneous ECG recording. The first major forward (toward the heart) waveform following the QRS complex of the ECG was designated as the systolic wave (S wave). A second major forward waveform starting around the middle of the R-R interval was the diastolic wave (D wave). The reversal waveform after the P wave was the retrograde wave caused by atrial contraction (A wave) (Fig.

Table 1. *General parameters and UBM cardiac B-mode and M-mode measurements in Tbx5*$^{del/+}$ *mice and wild-type littermates*

Parameters	1 wk		2 wk		4 wk		8 wk	
	Wild-type	*Tbx5*$^{del/+}$	Wild-type	*Tbx5*$^{del/+}$	Wild-type	*Tbx5*$^{del/+}$	Wild-type	*Tbx5*$^{del/+}$
Body weight, g	6.1±0.1	5.6±0.1	9.5±0.3^{a}	8.9±0.4^{A}	19.7±0.5^{a,b}	19.0±0.5^{A,B}	29.1±1.0^{a,b,c}	27.8±1.1^{A,B,C}
Heart rate, beats/min	386±12	391±14	366±23	369±10	430±14^{b}	440±15^{B}	403±10	395±9
LV end diastole								
AW, mm	0.63±0.02	0.66±0.02	0.61±0.01	0.68±0.03	0.80±0.02^{a,b}	0.86±0.02^{A,B}	0.88±0.03^{a,b,c}	0.88±0.03^{A,B}
EDD, mm	2.48±0.05	2.42±0.07	3.16±0.03^{a}	2.83±0.07^{A}*	3.84±0.05^{a,b}	3.35±0.08^{A,B}*	4.35±0.09^{a,b,c}	3.76±0.10^{A,B,C}*
PW, mm	0.57±0.01	0.57±0.02	0.56±0.01	0.64±0.01^{A}*	0.64±0.01^{a,b}	0.76±0.02^{A,B}*	0.76±0.02^{a,b,c}	0.82±0.03^{A,B,C}
LV end systole								
AW, mm	0.94±0.03	0.94±0.03	0.91±0.03	0.95±0.03	1.20±0.03^{a,b}	1.21±0.03^{A,B}	1.22±0.05^{a,b}	1.20±0.04^{A,B}
ESD, mm	1.41±0.05	1.49±0.07	2.04±0.06^{a}	1.84±0.09^{A}	2.43±0.08^{a,b}	2.14±0.09^{A,B}	3.07±0.13^{a,b,c}	2.59±0.10^{A,B,C}*
PW, mm	0.84±0.02	0.77±0.03	0.81±0.02	0.85±0.03	0.98±0.02^{a,b}	1.03±0.03^{A,B}	1.00±0.03^{a,b}	1.03±0.04^{A,B}
LV FS, %	55.8±2.0	48.4±2.4	43.5±2.6^{a}	43.5±2.5	45.5±2.4^{a}	44.7±2.3	35.1±2.5^{a,b,c}	37.4±2.0^{A}
MPA diameter, mm	0.88±0.02	0.84±0.02	0.97±0.01^{a}	0.96±0.02^{A}	1.27±0.03^{a,b}	1.24±0.03^{A,B}	1.36±0.04^{a,b,c}	1.43±0.05^{A,B,C}

Values are means ± SE for 12 wild-type and 12 *Tbx5*$^{del/+}$ mice from 1 to 8 wk of age. AW, anterior wall thickness of left ventricle (LV); EDD, LV end-diastolic diameter; ESD, LV end-systolic diameter; FS, fractional shortening of LV; MPA, main pulmonary artery; PW, posterior wall thickness of LV; UBM, ultrasound biomicroscopy. Two-way repeated-measures ANOVA was used for data analysis, and the Student-Newman-Keuls method was used for pairwise multiple comparisons. Superscript letters a, b, and c represent significant differences from the corresponding parameters in wild-type littermates at 1, 2, and 4 wk of age, respectively. Superscript letters A, B, and C represent significant differences from the corresponding parameters in *Tbx5*$^{del/+}$ mice at 1, 2, and 4 wk of age, respectively. *$P < 0.02$ compared with corresponding value of wild-type littermates at the same age.

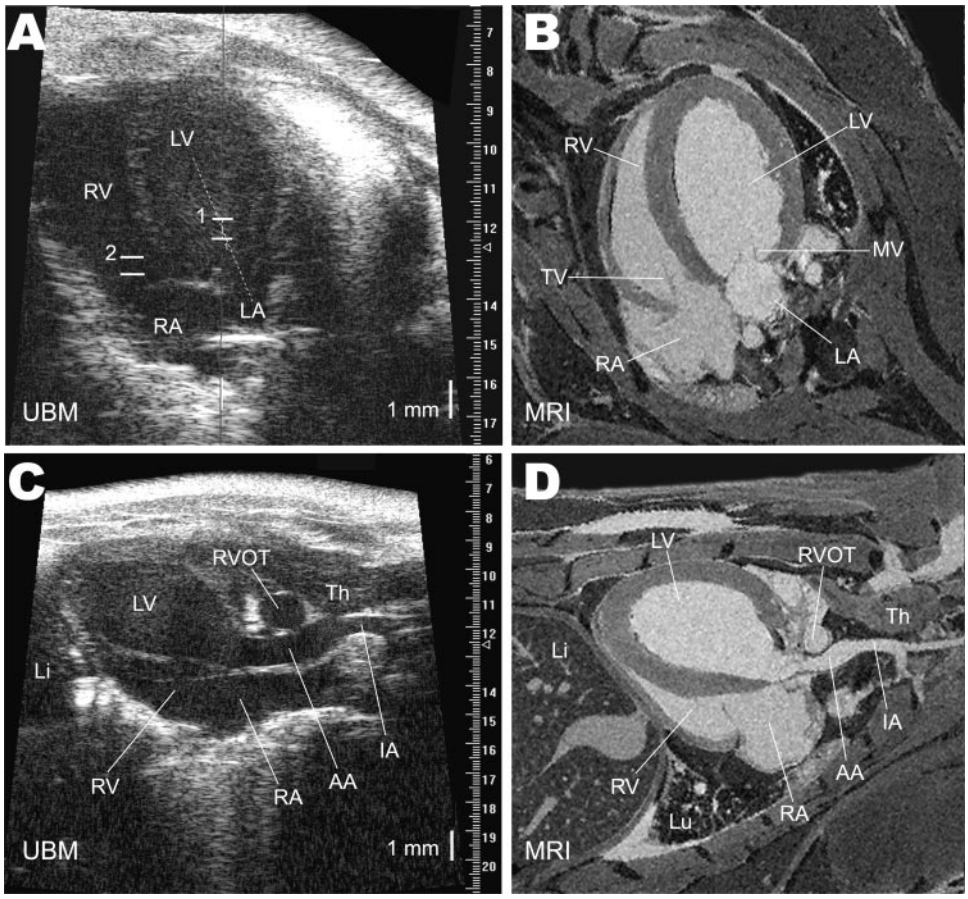

Fig. 1. Examples of in vivo cardiac imaging sections with ultrasound biomicroscopy (UBM) and anatomic confirmation by postmortem MRI. *A*: UBM image from the apical 4-chamber view in a wild-type mouse at 8 wk of age. Equal signs 1 and 2 represent the locations of Doppler sample volume for measuring the mitral flow and tricuspid flow, respectively. RV, right ventricle; LV, left ventricle; RA, right atrium; LA, left atrium. *B*: MRI image of a similar section as for UBM imaging in *A*. MV, mitral valve; TV, tricuspid valve. *C*: UBM image from a left parasternal longitudinal view showing the structure from the LV to the ascending aorta (AA), as well as the RA, the RV and the right ventricular outflow tract (RVOT). IA, innominate artery; Li, liver; Th, thymus. *D*: MRI image of a similar section as for UBM imaging in *C*. Lu, lung.

3, *C* and *D*). The peak flow velocities of all these Doppler waveforms were measured, and the measurements from three consecutive cardiac cycles were averaged.

Quantification of Tbx5 *Gene Expression in Ventricular Myocardium*

In *group II*, immediately after the in vivo UBM observation, the mice were killed, the hearts were excised, and the atria and ventricles were dissected. Total RNA was extracted from the ventricular myocardium with TRIzol (Invitrogen) and analyzed for purity and concentration on an Ultrospec 3000 (Pharmacia Biotech). One to five micrograms of RNA was reverse transcribed with the Supercript First Strand RT-PCR Synthesis System (Invitrogen) with oligo(dT) primers. Subsequently, quantitative real-time PCR was performed with the ABI 7000 Sequence Detector (Applied Biosystems, Foster City, CA). Gene expression was quantified with customized Assays-on-Demand (Applied Biosystems) for *Tbx5*. Gene expression data were normalized with Taqman rodent glyceraldehyde phosphate dehydrogenase (Applied Biosystems).

Postmortem Cardiac Anatomic Confirmation

In situ cardiac MRI on fixed mice. After UBM examination at 8 wk, all mice in *group I* were perfused with gadopentetate dimeglumine (Magnevist, Berlex Canada, Pointe Claire, QC, Canada) and fixed by infusion of formalin for whole body MRI (18, 37). MRI was conducted with a 40-cm bore, 7-T magnet (Magnex Scientific, Oxford, UK) controlled by a UnityInova console (Varian NMR Instruments, Palo Alto, CA) as previously described (2). We used a conventional spin echo pulse sequence with the following imaging parameters: 650-ms repetition time, 16.5-ms echo time, 97-mm × 27-mm × 27-mm field of view, and 970 × 270 × 270 imaging matrix providing isotropic voxels of 100-μm resolution. After reconstruction of the raw data, a three-dimensional MRI data set was visualized, processed, and analyzed with Amira software (TGS, San Diego, CA). By manipulating a plane in the three-dimensional data set, the sections corresponding to the in vivo UBM imaging views were carefully analyzed for comparative assignments of the cardiac structures (Fig. 1, *B* and *D*; Ref. 38). The relative size of four cardiac chambers was qualitatively evaluated, and the atrial and ventricular septa were carefully observed to identify the presence of any defects (Fig. 2, *C* and *D*).

Dissection of heart. The heart specimens of 12 $Tbx5^{del/+}$ mice were dissected. The external shape of the heart and the relative sizes of the atria and ventricles were qualitatively evaluated. The right atrium and ventricle were then cut, and the atrial and ventricular septa were observed from the right side. For area measurement, a plastic mesh with a known area of each square was placed beside the dissected heart specimen under the microscope and digitally photographed. The atrial septum was made as flat as possible, but excessive stretching was avoided. With Adobe Photoshop 7.0, the image pixel number was measured for each square of the plastic mesh and the area of each pixel was calculated. The heart defects were then manually traced for counting the pixel numbers, and the areas of defects were calculated.

Statistics

Differences between $Tbx5^{del/+}$ mice and wild-type littermates and changes of parameters with age were analyzed with two-way repeated-measures ANOVA. The Student-Newman-Keuls method was used for all pairwise multiple comparisons (SigmaStat, Statistical Solutions). The relations among the size of the ASDs, the *Tbx5* expression level in ventricular myocardium, and the parameters obtained by UBM imaging were analyzed by linear regression. All data

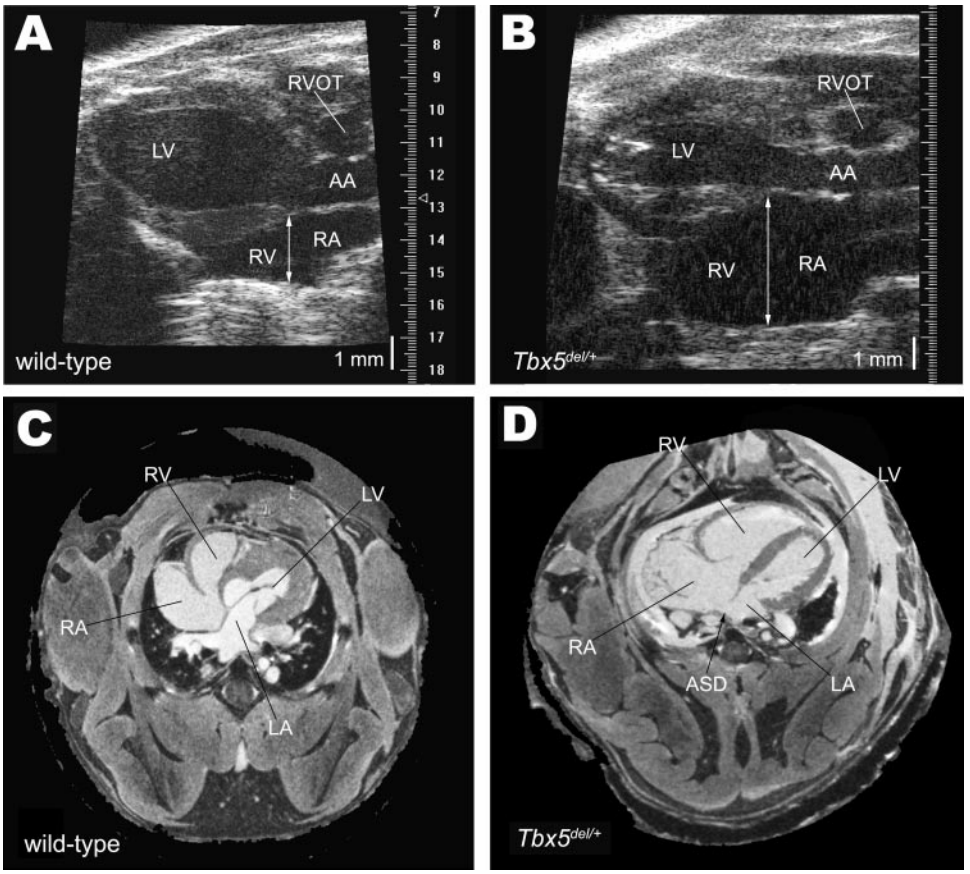

Fig. 2. Images of in vivo UBM and postmortem MRI on *Tbx5*$^{del/+}$ mice and wild-type littermates at 8 wk of age. *A*: UBM cardiac image of a wild-type littermate from the left parasternal longitudinal section, showing the left ventricular outflow tract in contrast with the right heart. *B*: UBM cardiac image of a *Tbx5*$^{del/+}$ mouse from the same imaging section as for *A*, showing the dilated RA and RV. White line with double arrows indicates the width of the tricuspid ring. *C*: MRI cardiac image of a wild-type littermate, showing normal overall shape and chamber size, as well as normal structures including continuous interatrial septum. *D*: MRI cardiac image of a *Tbx5*$^{del/+}$ mouse, showing dilated RA and RV and an atrial septal defect (ASD).

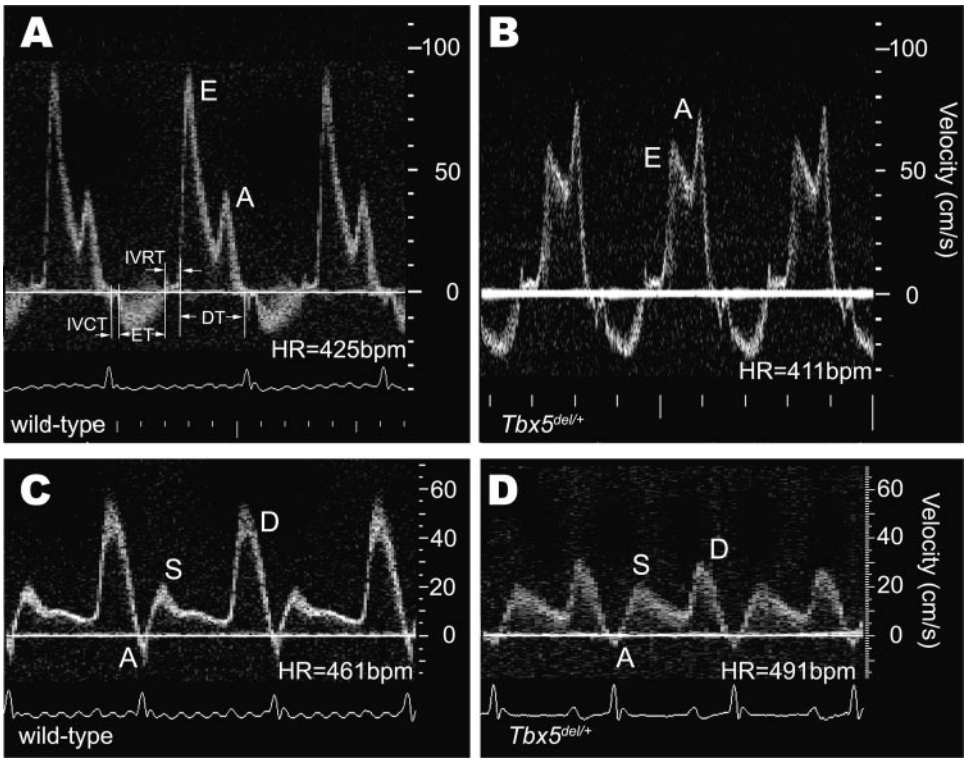

Fig. 3. Typical Doppler flow spectra recorded from the mitral orifice and pulmonary vein in *Tbx5*$^{del/+}$ mice and wild-type littermates. *A*: mitral Doppler spectrum of a wild-type littermate (8 wk) showing a higher early ventricular filling wave (E wave) and a lower late filling wave caused by atrial contraction (A wave). The methods of measuring the left ventricular systolic and diastolic intervals are demonstrated. IVCT, isovolumic contraction time; IVRT, isovolumic relaxation time; ET, ejection time; DT, diastolic filling time; HR, heart rate. *B*: mitral Doppler flow spectrum of a *Tbx5*$^{del/+}$ mouse (8 wk) showing the reversal of the relative amplitudes of the E and A waves. *C*: pulmonary venous Doppler flow spectrum of a wild-type littermate (4 wk) showing a normal flow pattern with lower systolic wave (S wave), a higher diastolic wave (D wave), and a small retrograde wave caused by atrial contraction (A wave). *D*: pulmonary venous Doppler flow spectrum of a *Tbx5*$^{del/+}$ mouse (4 wk) showing a significantly decreased D wave as well as a small A wave.

are expressed as means ± SE, and statistical significance was set at $P < 0.02$.

RESULTS

Mouse body weight increased with postnatal development, but no significant difference was found between *Tbx5*$^{del/+}$ mice and wild-type littermates at any age. Heart rate varied between 1 and 8 wk of age but did not demonstrate any consistent trend with postnatal development or show any difference between *Tbx5*$^{del/+}$ mice and wild-type littermates (Table 1).

B-mode UBM imaging clearly visualized the overall morphology of the heart and the cardiac structures of the studied mice (Fig. 1, *A* and *C*). A significant dilatation of right atrium and ventricle was found in *Tbx5*$^{del/+}$ mice compared with wild-type littermates at all ages studied (Fig. 2, *A* and *B*). The size of the left atrium was less well defined because of its irregular shape and the lack of an appropriate imaging section, and the ASDs were not well visualized by UBM.

The mitral Doppler flow spectrum showed a significantly reduced peak E velocity after 2 wk of age and an increased peak A velocity after 1 wk in *Tbx5*$^{del/+}$ mice compared with those in wild-type littermates (Figs. 3, *A* and *B*, and 4, *A* and *B*). Consequently, whereas the peak E-to-A ratio in the wild-type mice increased rapidly from 1 to 4 wk of age and stayed at ~2 afterwards, the corresponding parameter of *Tbx5*$^{del/+}$ mice showed little increase from neonatal to juvenile periods but remained at ~1 (Fig. 4*C*). The peak E/A of *Tbx5*$^{del/+}$ mice became <1 from 4 wk of age, suggesting the general reversal of the relative amplitudes of the E and A waveforms as shown in Fig. 3*B*. The mitral flow TVI of *Tbx5*$^{del/+}$ mice did not differ from that of wild-type littermates at any age, although it increased slightly from 4 to 8 wk of age in both strains (Fig. 4*D*). In analysis of the mitral flow, one *Tbx5*$^{del/+}$ mouse was excluded at 8 wk of age because of fused E and A waves caused by high heart rate.

The ratio of left ventricular IVRT to DT of *Tbx5*$^{del/+}$ mice was generally higher than that of wild-type littermates at all ages (Fig. 4*E*). However, the ratio of left ventricular IVCT to ET did not show any significant difference between the two strains at any age (Fig. 4*F*).

In the dilated tricuspid orifice, as indicated by the increased width of the tricuspid ring in *Tbx5*$^{del/+}$ mice, the total TVI of tricuspid flow significantly increased because of the increases of both E and A waveforms at all ages. However, the peak E/A did not demonstrate any significant change with age in either *Tbx5*$^{del/+}$ mice or wild-type littermates or any significant difference between the two strains (Fig. 5). One wild-type and two *Tbx5*$^{del/+}$ mice at 8 wk were excluded from the analysis of tricuspid flow spectrum because of fused E and A waves caused by high heart rate.

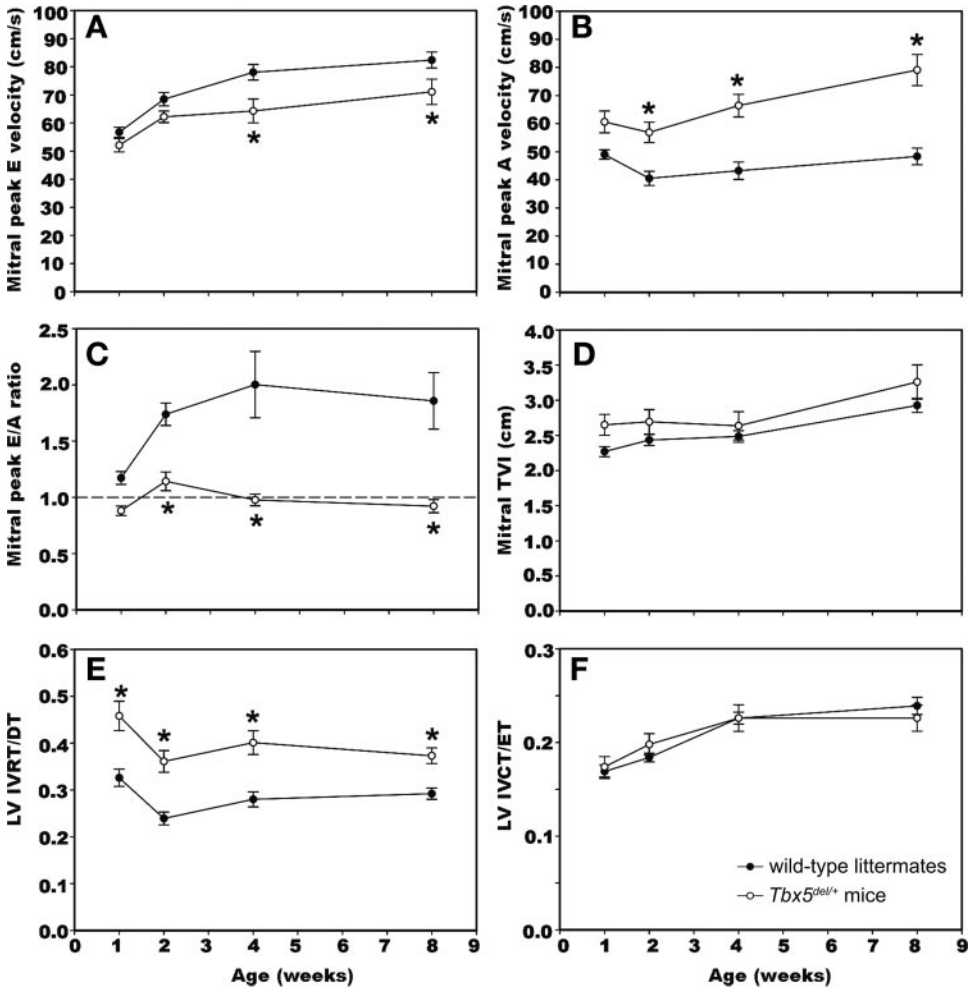

Fig. 4. Changes of the mitral Doppler flow parameters during postnatal development in *Tbx5*$^{del/+}$ mice compared with wild-type littermates. *A*: peak velocity of E wave. *B*: peak velocity of A wave. *C*: ratio of peak velocities of E wave to A wave (peak E/A). *D*: total time-velocity integral (TVI) of E and A waves. *E*: ratio of left ventricular IVRT to DT (LV IVRT/DT). *F*: ratio of left ventricular IVCT to ET (LV IVCT/ET). *$P < 0.02$ compared with corresponding parameter of wild-type littermates.

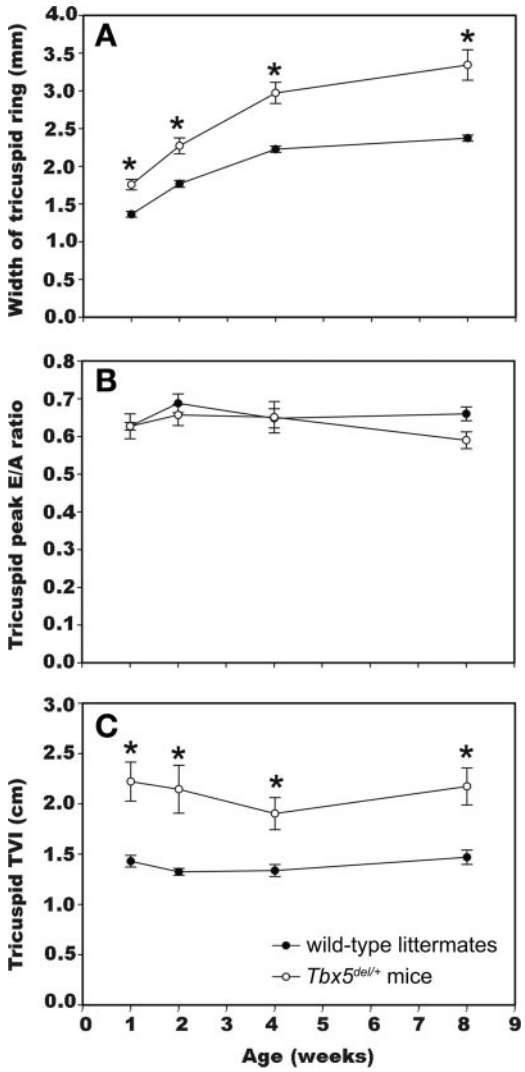

Fig. 5. Changes of the right heart dimension and tricuspid Doppler flow parameters during postnatal development in *Tbx5*$^{del/+}$ mice and wild-type littermates. *A*: width of tricuspid ring. *B*: ratio of peak velocities of E wave to A wave of the tricuspid Doppler flow spectrum (peak E/A). *C*: total TVI of E and A waves. *$P < 0.02$ compared with corresponding parameter of wild-type littermates.

The pulmonary venous Doppler flow spectrum showed significantly increased S waves, decreased D waves, and also reduced retrograde A waves in *Tbx5*$^{del/+}$ mice compared with those in wild-type littermates at most age points (Figs. 3, *C* and *D* and 6, *A*, *C*, and *E*). The Doppler flow spectrum from the right superior vena cava showed generally reduced D waves in *Tbx5*$^{del/+}$ mice compared with wild-type littermates. However, the significant decrease of S waves and increase of retrograde A waves started to occur at 8 wk of age in *Tbx5*$^{del/+}$ mice (Fig. 6, *B*, *D*, and *F*).

Left ventricular wall thicknesses and chamber dimensions significantly increased with age, as would be expected (Table 1). End-diastolic ventricular wall thickness of *Tbx5*$^{del/+}$ mice was occasionally greater than that of wild-type littermates. However, there was no significant difference in end-systolic ventricular wall thickness between the two strains at any age. In *Tbx5*$^{del/+}$ mice, the left ventricular end-diastolic chamber diameter from 2 to 8 wk of age and the end-systolic chamber diameter at 8 wk were significantly smaller than the corresponding values in wild-type littermates. Left ventricular fractional shortening showed a slight decrease with advancing age in both strains, but no significant difference was found between the two strains at any age.

With MRI, ASDs were found in 7 of 12 *Tbx5*$^{del/+}$ mice (Fig. 2*D*). Of the other five *Tbx5*$^{del/+}$ mice, ASD was not seen in two mice and the atrial septum was poorly visualized because of atrial collapse or an artifact caused by air bubbles introduced during perfusion in three mice. Dissection of the hearts, which were fixed in situ, enabled direct observation of the atrial and ventricular septa in all mice and yielded results that were more reliable than those from MRI. ASDs were clearly identified in 8 of 12 *Tbx5*$^{del/+}$ mice, and the average area of the defects was 1.4 ± 0.5 mm^2. In these eight mice, the area of ASD was significantly correlated with width of the tricuspid ring ($r = 0.95$, $P < 0.01$), mitral peak E/A ($r = -0.88$, $P < 0.01$), and left ventricular IVRT normalized to cardiac cycle length ($r = 0.82$, $P < 0.02$) at 8 wk of age. When the four *Tbx5*$^{del/+}$ mice without observable ASDs were included in the analysis with the defect area defined as zero, significant correlation was also found between the defect size and width of the tricuspid ring, as well as left ventricular IVRT/DT at 8 wk of age (Fig. 7). Contrary to what was expected, the width of the tricuspid ring of the four *Tbx5*$^{del/+}$ mice without observable ASDs did not differ significantly from that of eight *Tbx5*$^{del/+}$ mice with ASDs at any age but was significantly greater than that of wild-type littermates at all ages. No ventricular septal defect was found in any *Tbx5*$^{del/+}$ mice.

In *group II*, average *Tbx5* mRNA in ventricular myocardium of *Tbx5*$^{del/+}$ mice was $47 \pm 5\%$ of that of wild-type littermates. Significant correlations were found between the *Tbx5* expression level in ventricular myocardium and size of the right heart, as well as the left ventricular diastolic filling parameters (Fig. 8).

DISCUSSION

Left Ventricular Diastolic Dysfunction in Tbx5$^{del/+}$ *Mice*

The present study demonstrates left ventricular diastolic dysfunction in *Tbx5*$^{del/+}$ mice as manifested by decreased mitral E waves, greatly increased A waves, and consequently reduced or reversed peak E-to-A ratios. Furthermore, the significant prolongation of the left ventricular IVRT precedes the changes of the E wave and the peak E/A and is readily detectable as early as the first week after birth. However, in the dilated tricuspid orifice of *Tbx5*$^{del/+}$ mice, although the peak velocities increase, the peak E/A remain unchanged and are similar to those of wild-type littermates during postnatal development.

Consistent with our previous studies (38, 39), the current results also demonstrate significantly different diastolic filling patterns between the right and left ventricles during postnatal development in wild-type mice. Abnormal left ventricular filling patterns have been observed previously in various mouse models. Mitral peak E/A were found to increase in hyperthyroid mice and decrease in senescent mice (31). In phospholamban-deficient mice, the mitral peak E velocity was found to increase but with the peak E/A unchanged (14). However, mitral flow with reversed amplitudes of the E and A

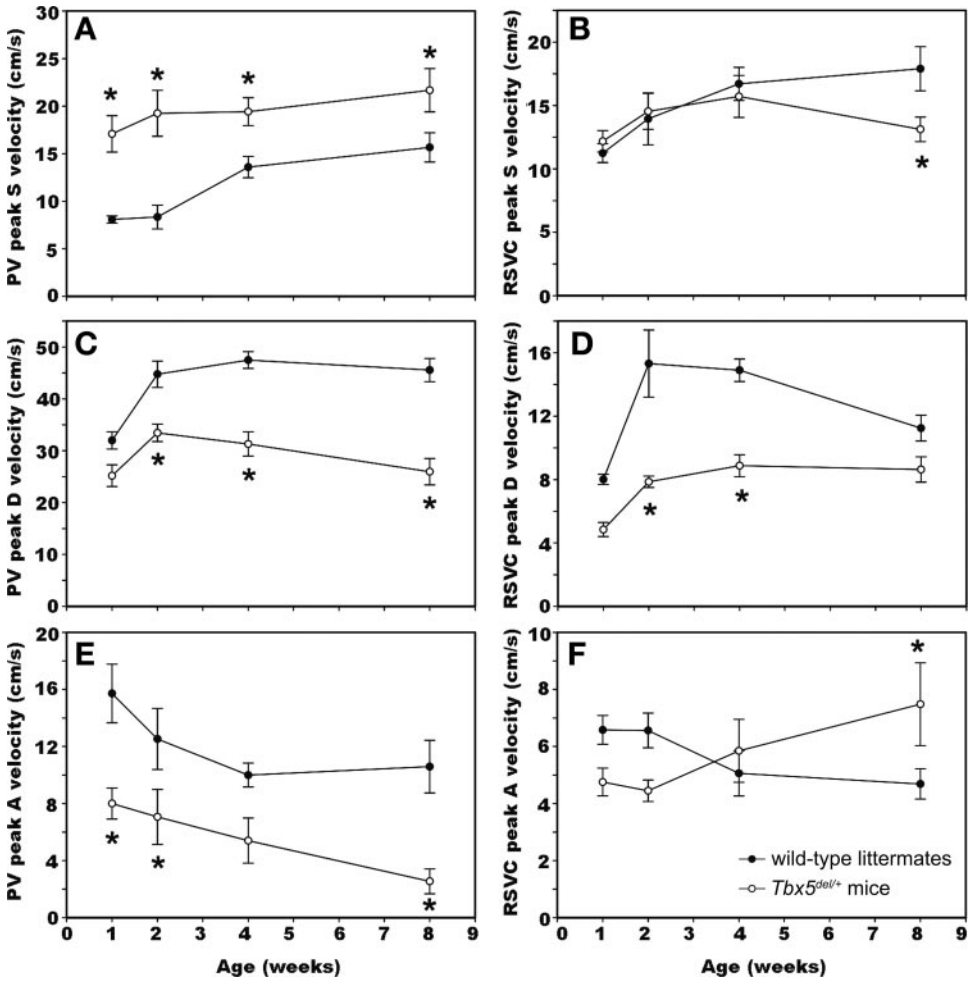

Fig. 6. Changes of the Doppler flow patterns in the left and right atrial inflow channels during postnatal development in $Tbx5^{del/+}$ mice and wild-type littermates. *A*: peak velocity of systolic wave (S wave) of the pulmonary vein (PV). *B*: peak velocity of S wave of the right superior vena cava (RSVC). *C*: peak velocity of diastolic wave (D wave) of PV. *D*: peak velocity of D wave of RSVC. *E*: peak velocity of retrograde A wave of PV. *F*: peak velocity of retrograde A wave of RSVC. $*P < 0.02$ compared with the corresponding parameter of the wild-type littermates.

waves, as observed in $Tbx5^{del/+}$ mice in the current study, has not previously been reported.

This study also demonstrates the changes in pulmonary venous flow pattern secondary to impaired left ventricular diastolic filling in mice. In the human pulmonary vein, the D wave is usually lower than the S wave in normal subjects and decreases when left ventricular diastolic filling is impaired (24). However, the D wave is normally higher than the S wave in wild-type mice (38) and dramatically decreases, corresponding to the reduced mitral E wave in $Tbx5^{del/+}$ mice.

Because of ASD in $Tbx5^{del/+}$ mice, the direction of the shunting through the septum may complicate the interpretation of the ventricular filling patterns. In $Tbx5^{del/+}$ mice, the increased peak E and A velocities and TVI in a dilated tricuspid orifice suggest the existence of volume overload in the right heart due to a left-to-right shunting, as customarily seen in humans with ASD (19, 30, 34). On the other hand, a generally reduced retrograde A wave in the pulmonary vein suggests that the pressure in the left atrium is not elevated. Moreover, the shunting in the opposite direction, e.g., right to left, would be expected to affect long-term growth because of hypoxemia, which is not the case in this study as indicated by the body weight of $Tbx5^{del/+}$ mice. Previous human data also suggest that the right-to-left shunting is rare in patients with ASD (~13%), and this is true even in older patients with severe pulmonary arterial hypertension (19, 30).

Whereas left ventricular diastolic function is deteriorated, the systolic contractile function of $Tbx5^{del/+}$ mice remains normal as indicated by the left ventricular fractional shortening and systolic time intervals. This finding is consistent with that in humans with ASD (3, 6). This result also explains the fact that the long-term growth of *Tbx5* mutants is not affected, probably because the normal systemic cardiac output is maintained. Our results also further conform to the finding in humans that ventricular diastolic dysfunction often precedes the onset of systolic dysfunction and contributes to the symptoms of various cardiac diseases (6, 24).

Possible Mechanisms for Left Ventricular Diastolic Dysfunction

Although the left ventricular wall thickness of $Tbx5^{del/+}$ mice was occasionally greater than that of wild-type littermates, there was no overwhelming evidence of general ventricular hypertrophy as an explanation of ventricular diastolic dysfunction.

According to the present data from mice and the knowledge obtained from humans, ASD and the consequent right heart dilatation may be one of the important factors responsible for the changes of the inflow patterns in the left heart of $Tbx5^{del/+}$ mice. In humans with ASD, right ventricular dilatation significantly alters left ventricular geometry (e.g., a flattened inter-

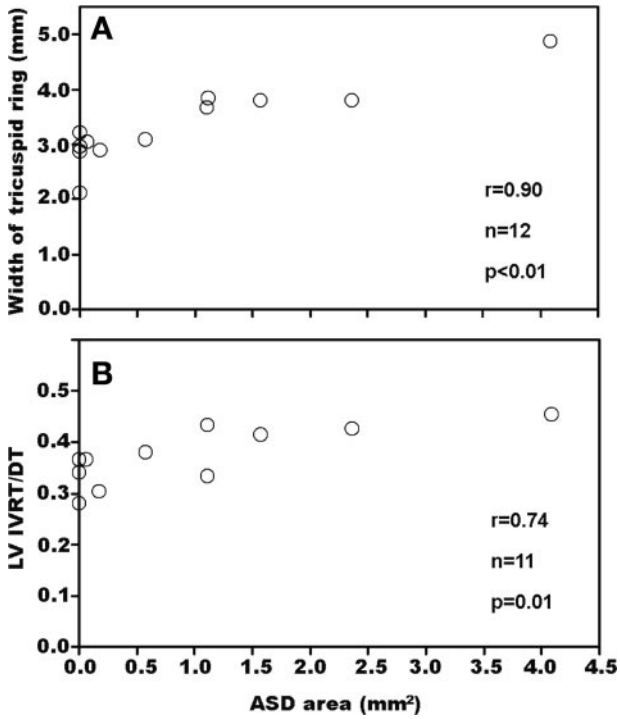

Fig. 7. Correlations between the size of the ASD and the width of the tricuspid ring (*A*) as well as the LV IVRT/DT (*B*) in 12 *Tbx5*$^{del/+}$ mice at 8 wk of age. Note that in 4 *Tbx5*$^{del/+}$ mice without observable ASD the areas of defects are arbitrarily defined as zero (points on the vertical axis). In measurement of the LV IVRT/DT from the mitral Doppler spectrum, 1 case is excluded because of the inappropriate quality of the recording.

ventricular septum toward the left ventricle at end systole and early diastole and decreased left ventricular chamber dimension), increases left ventricular chamber stiffness and reduces its compliance, and consequently impairs left ventricular filling (3, 6, 17). However, all these abnormalities are not associated with significant changes in the mitral flow pattern in patients with normal pulmonary pressure (21, 30, 34). Human patients with similar right ventricular enlargement but normal to moderately elevated pulmonary pressure do not have mitral flow patterns significantly different from those in normal subjects. Only in a small group of patients (~19%, >25 yr of age) with severe pulmonary hypertension is the mitral peak E/A reversed to <1 (30). Therefore, it is believed that left ventricular diastolic dysfunction is not simply due to right ventricular enlargement caused by volume overload but is more likely attributed to a disturbance of left ventricular isovolumic relaxation related to severe right ventricular pressure overload. The high pressure in the right ventricle delays the decline of the right ventricular tension and therefore interferes with the early active relaxation of the left ventricle. In our study, the mitral flow pattern of *Tbx5*$^{del/+}$ mice is very similar to that of human patients with both right ventricular dilatation and severe pulmonary hypertension, which are usually developed during adulthood. Unfortunately, the pulmonary pressure was not measured in this study, and the existence of right ventricular pressure overload cannot be confirmed. In the superior vena cava, the general decrease of the D wave, the gradual decrease of the S wave, and the increase of the retrograde A wave with advancing age suggest a gradual building up of pressure in the right heart during postnatal development. However, the fact that the diameter of the main pulmonary arterial trunk is not different between two strains of mice from the neonatal period to early adulthood does not suggest the existence of severe pulmonary arterial hypertension.

Compared with humans, significant change of the mitral flow pattern in *Tbx5*$^{del/+}$ mice occurs at a relatively younger age (neonatal to juvenile periods) and was quite consistent among the studied individuals. Even in mice with relatively small ASDs, the change in mitral flow pattern is significant compared with that in wild-type littermates. Moreover, the prolongation of IVRT, which is closely related to the left ventricular myocardial active relaxation during early diastole, is detectable early in neonates. One possible reason is that the mouse, as a species functioning at a much higher heart rate than humans, may have less reserve. However, considering the significant correlation between the *Tbx5* expression level in

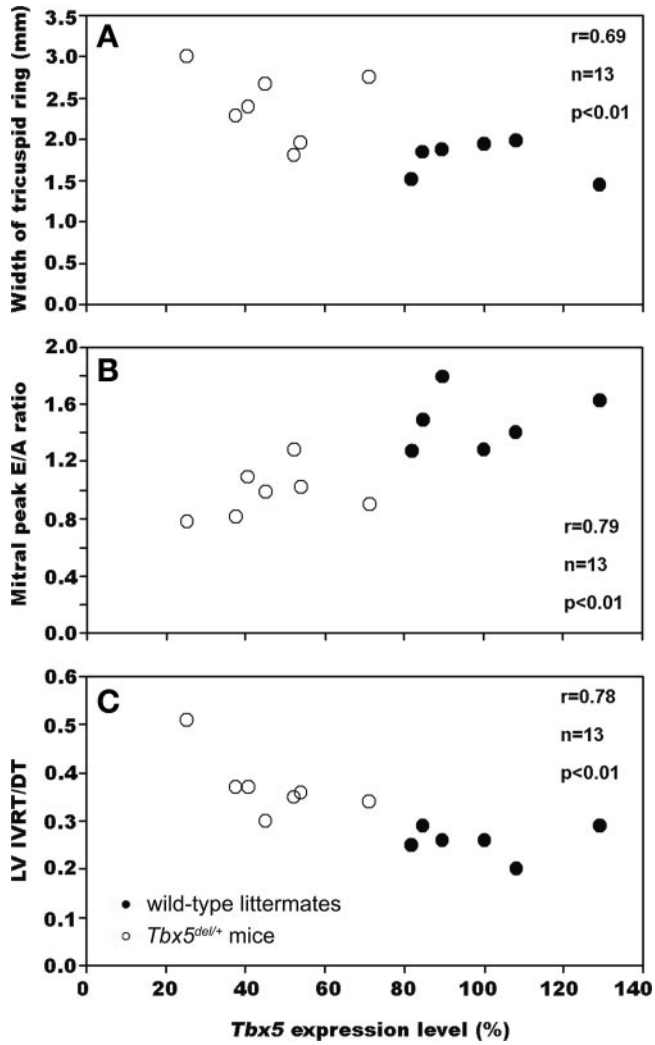

Fig. 8. Correlations between the *Tbx5* expression level in the ventricular myocardium and the parameters of the right heart dimension as well as the left ventricular diastolic filling pattern in a group of mice (7 *Tbx5*$^{del/+}$, 6 wild type) at 2 wk of age. *A*: correlations between the *Tbx5* expression level and the width of the tricuspid ring. *B*: correlations between the *Tbx5* expression level and the mitral peak E/A. *C*: correlations between the *Tbx5* expression level and the LV IVRT/DT. On the horizontal axis, 100% corresponds to the average expression level of wild-type mice.

ventricular myocardium and the left ventricular diastolic filling parameters, it is necessary to find out whether the *Tbx5* mutation contributes to left ventricular diastolic dysfunction by directly affecting the ventricular myocardial properties. We speculate that the *Tbx5* haploinsufficiency may affect expression of downstream targeted genes required in left ventricular development for normal myocardial function. A ventricle-specific deletion of *Tbx5*, which would eliminate the presence of ASDs, will be helpful for elucidating the role of *Tbx5* gene expression in the deterioration of ventricular function. The failure to find an ASD in four $Tbx5^{del/+}$ mice probably results from the defect being too small or at an unusual location other than the central part of the septum, because the increased right heart dimensions suggest right-sided volume overload, which is indicative of the existence of left-to-right shunting.

Limitations

Isoflurane was used to anesthetize the mice for stable data acquisition. Although the previously published data about the effect of isoflurane on cardiac function are controversial, most studies in healthy children (13), in dogs (36), and in chick embryos (35) suggest that isoflurane at a low dose does not significantly change ventricular relaxation and myocardial compliance, and it produces less myocardial depression than other volatile anesthetics. More specifically, in our previous study (39), mice at ~1–2 wk of age were observed with and without anesthesia by isoflurane. The diastolic filling patterns (peak E/A) for both right and left ventricles did not show significant differences (39). Therefore, isoflurane at the low concentration level of ~1.5% is assumed to have a minimal effect on ventricular diastolic function in the present study.

Although body temperature was carefully maintained, the mouse heart rate under anesthesia was generally lower than that of awake and resting adult mice (~540 bpm) measured by chronic catheterization (8). However, compared with other commonly used intraperitoneally injected anesthetics, isoflurane has a minimal effect on the mouse heart rate (41). Relative to the previously reported heart rates (from ~230 to ~275 bpm on average) in anesthetized adult wild-type mice (14, 26, 32), the heart rate in our study was closer to that of awake mice. The variation of heart rate may change the relative amplitudes of E and A waveforms. The A wave will decrease relative to the E wave when heart rate decreases (24). However, in $Tbx5^{del/+}$ mice, the A wave was always significantly higher than that of the wild-type littermates, even with the decreased heart rate. Moreover, when $Tbx5^{del/+}$ mice and wild-type littermates were compared at the same age, heart rate did not differ between strains. Therefore, the decrease and variation of the heart rate should not affect the interpretation of the data nor preclude us from making our conclusions.

The MRI observation in this study was purely qualitative. It provided definitive confirmation of the structures visualized in vivo with UBM. It was also used as a means of evaluating the cardiac anatomy, including the continuity of the atrial and ventricular septa. However, any quantitative measurements of the fixed mouse heart obtained by MRI would not be comparable with those from in vivo UBM imaging because of the lack of physiological pressure in the fixed heart, and therefore such measurements were not conducted. Dynamic cardiac MRI on live mice is under development in our laboratory to provide in vivo quantitative cardiac measurements for morphological and functional phenotyping in future studies.

In conclusion, this study using high-frequency ultrasound imaging reveals various cardiac functional phenotypes of $Tbx5^{del/+}$ mice, which are detectable in neonates and continue to deteriorate with advancing age during postnatal development. Left ventricular diastolic function is significantly degraded as indicated by the changes in mitral and pulmonary venous Doppler flow patterns, whereas left ventricular systolic function remains normal. Right heart volume overload due to ASD is observed, but right ventricular diastolic function is unchanged. The right heart dilatation alone is not sufficient for a full explanation of the underlying mechanisms responsible for the left ventricular diastolic dysfunction. In future studies, a ventricle-specific deletion of *Tbx5*, which would eliminate ASDs, will be helpful for elucidating the effect of *Tbx5* gene expression on ventricular myocardial function during cardiac development.

ACKNOWLEDGMENTS

The authors thank Jun Dazai for technical support.

GRANTS

This work is part of the Mouse Imaging Centre (MICe) at the Hospital for Sick Children and the University of Toronto. The infrastructure was funded by the Canada Foundation for Innovation (CFI) and Ontario Innovation Trust (OIT). The research was funded by an Ontario Research and Development Challenge Fund (ORDCF) grant to the Ontario Consortium for Small Animal Imaging (OCSAI) and also the Heart & Stroke Foundation of Ontario.

DISCLOSURES

F. S. Foster acknowledges a financial interest in VisualSonics Inc. Y.-Q. Zhou consults for VisualSonics Inc.

REFERENCES

1. **Basson CT, Bachinsky DR, Lin RC, Levi T, Elkins JA, Soults J, Grayzel D, Kroumpouzou E, Traill TA, Leblanc-Straceski J, Renault B, Kucherlapati R, Seidman JG, and Seidman CE.** Mutations in human *TBX5* cause limb and cardiac malformation in Holt-Oram syndrome. *Nat Genet* 15: 30–35, 1997.
2. **Bock NA, Konyer NB, and Henkelman RM.** Multiple-mouse MRI. *Magn Reson Med* 49: 158–167, 2003.
3. **Booth DC, Wisenbaugh T, Smith M, and DeMaria AN.** Left ventricular distensibility and passive elastic stiffness in atrial septal defect. *J Am Coll Cardiol* 12: 1231–1236, 1988.
4. **Bruneau BG, Logan M, Davis N, Levi T, Tabin CJ, Seidman JG, and Seidman CE.** Chamber-specific cardiac expression of Tbx5 and heart defects in Holt-Oram syndrome. *Dev Biol* 211: 100–108, 1999.
5. **Bruneau BG, Nemer G, Schmitt JP, Charron F, Robitaille L, Caron S, Conner DA, Gessler M, Nemer M, Seidman CE, and Seidman JG.** A murine model of Holt-Oram syndrome defines roles of the T-box transcription factor Tbx5 in cardiogenesis and disease. *Cell* 106: 709–721, 2001.
6. **Carabello BA, Gash A, Mayers D, and Spann JF.** Normal left ventricular systolic function in adults with atrial septal defect and left heart failure. *Am J Cardiol* 49: 1868–1873, 1982.
7. **Collins KA, Korcarz CE, and Lang RM.** Use of echocardiography for the phenotypic assessment of genetically altered mice. *Physiol Genomics* 13: 227–239, 2003.
8. **Desai KH, Sato R, Schauble E, Barsh GS, Kobilka BK, and Bernstein D.** Cardiovascular indexes in the mouse at rest and with exercise: new tools to study models of cardiac disease. *Am J Physiol Heart Circ Physiol* 272: H1053–H1061, 1997.
9. **Eidem BW, Tei C, O'Leary PW, Cetta F, and Seward JB.** Nongeometric quantitative assessment of right and left ventricular function: myocardial performance index in normal children and patients with Ebstein anomaly. *J Am Soc Echocardiogr* 11: 849–856, 1998.

10. **Fatkin D, Christe ME, Aristizabal O, McConnell BK, Srinivasan S, Schoen FJ, Seidman CE, Turnbull DH, and Seidman JG.** Neonatal cardiomyopathy in mice homozygous for the Arg403Gln mutation in the α cardiac myosin heavy chain gene. *J Clin Invest* 103: 147–153, 1999.
11. **Foster FS, Pavlin CJ, Harasiewicz KA, Christopher DA, and Turnbull DH.** Advances in ultrasound biomicroscopy. *Ultrasound Med Biol* 26: 1–27, 2000.
12. **Foster FS, Zhang MY, Zhou YQ, Liu G, Mehi J, Cherin E, Harasiewicz KA, Starkoski BG, Zan L, Knapik DA, and Adamson SL.** A new ultrasound instrument for in vivo microimaging of mice. *Ultrasound Med Biol* 28: 1165–1172, 2002.
13. **Gallagher TM, Shields MD, and Black GW.** Isoflurane does not reduce aortic peak flow velocity in children. *Br J Anaesth* 58: 1116–1121, 1986.
14. **Hoit BD, Khoury SF, Kranias EG, Ball N, and Walsh RA.** In vivo echocardiographic detection of enhanced left ventricular function in gene-targeted mice with phospholamban deficiency. *Circ Res* 77: 632–637, 1995.
15. **Holt M and Oram S.** Familial heart disease with skeletal malformations. *Br Heart J* 22: 236–242, 1960.
16. **Huang T.** Current advances in Holt-Oram syndrome. *Curr Opin Pediatr* 14: 691–695, 2002.
17. **Iwasaki Y, Satomi G, and Yasukochi S.** Analysis of ventricular septal motion by doppler tissue imaging in atrial septal defect and normal heart. *Am J Cardiol* 83: 206–210, 1999.
18. **Johnson GA, Cofer GP, Gewalt SL, and Hedlund LW.** Morphologic phenotyping with MR microscopy: the visible mouse. *Radiology* 222: 789–793, 2002.
19. **Konstantinides S, Geibel A, Kasper W, and Just H.** The natural course of atrial septal defect in adults—a still unsettled issue. *Klin Wochenschr* 69: 506–510, 1991.
20. **Larrazet F, Pellerin D, Fournier C, Witchitz S, and Veyrat C.** Right and left isovolumic ventricular relaxation time intervals compared in patients by means of a single-pulsed Doppler method. *J Am Soc Echocardiogr* 10: 699–706, 1997.
21. **Lavine SJ, Tami L, and Jawad I.** Pattern of left ventricular diastolic filling associated with right ventricular enlargement. *Am J Cardiol* 62: 444–448, 1988.
22. **Mori AD and Bruneau BG.** TBX5 mutations and congenital heart disease: Holt-Oram syndrome revealed. *Curr Opin Cardiol* 19: 211–215, 2004.
23. **Moskowitz IP, Pizard A, Patel VV, Bruneau BG, Kim JB, Kupershmidt S, Roden D, Berul CI, Seidman CE, and Seidman JG.** The T-Box transcription factor Tbx5 is required for the patterning and maturation of the murine cardiac conduction system. *Development* 131: 4107–4116, 2004.
24. **Nishimura RA, Abel MD, Hatle LK, and Tajik AJ.** Assessment of diastolic function of the heart: background and current applications of Doppler echocardiography. II. Clinical studies. *Mayo Clin Proc* 64: 181–204, 1989.
25. **Phoon CK and Turnbull DH.** Ultrasound biomicroscopy-Doppler in mouse cardiovascular development. *Physiol Genomics* 14: 3–15, 2003.
26. **Pollick C, Hale SL, and Kloner RA.** Echocardiographic and cardiac Doppler assessment of mice. *J Am Soc Echocardiogr* 8: 602–610, 1995.
27. **Quinones MA, Otto CM, Stoddard M, Waggoner A, and Zoghbi WA.** Recommendations for quantification of Doppler echocardiography: a report from the Doppler Quantification Task Force of the Nomenclature and Standards Committee of the American Society of Echocardiography. *J Am Soc Echocardiogr* 15: 167–184, 2002.
28. **Sahn DJ, DeMaria A, Kisslo J, and Weyman A.** Recommendations regarding quantitation in M-mode echocardiography: results of a survey of echocardiographic methods. *Circulation* 58: 1072–1083, 1978.
29. **Schiller NB, Shah PM, Crawford M, DeMaria A, Devereux R, Feigenbaum H, Gutgesell H, Reichek N, Sahn D, and Schnittger I.** Recommendations for quantitation of the left ventricle by two-dimensional echocardiography. American Society of Echocardiography Committee on Standards. Subcommittee on Quantitation of Two-Dimensional Echocardiograms. *J Am Soc Echocardiogr* 2: 358–367, 1989.
30. **Stojnic B, Krajcer Z, Pavlovic P, Nozic M, Aleksandrov R, and Prcovic M.** Pulsed Doppler assessment of left ventricular diastolic function in atrial septal defect. *Tex Heart Inst J* 19: 258–264, 1992.
31. **Taffet GE, Hartley CJ, Wen X, Pham T, Michael LH, and Entman ML.** Noninvasive indexes of cardiac systolic and diastolic function in hyperthyroid and senescent mouse. *Am J Physiol Heart Circ Physiol* 270: H2204–H2209, 1996.
32. **Tanaka N, Dalton N, Mao L, Rockman HA, Peterson KL, Gottshall KR, Hunter JJ, Chien KR, and Ross J Jr.** Transthoracic echocardiography in models of cardiac disease in the mouse. *Circulation* 94: 1109–1117, 1996.
33. **Tei C, Nishimura RA, Seward JB, and Tajik AJ.** Noninvasive Doppler-derived myocardial performance index: correlation with simultaneous measurements of cardiac catheterization measurements. *J Am Soc Echocardiogr* 10: 169–178, 1997.
34. **Veyrat C, Legeais S, Sainte-Beuve D, and Kalmanson D.** Color and pulsed Doppler studies of atrial flow dynamics in normals and adult patients with uncomplicated atrial septal defects. *Int J Card Imaging* 6: 1–9, 1990–1991.
35. **Wojtczak JA.** The hemodynamic effects of halothane and isoflurane in chick embryo. *Anesth Analg* 90: 1331–1335, 2000.
36. **Yamada T, Takeda J, Koyama K, Sekiguchi H, Fukushima K, and Kawazoe T.** Effects of sevoflurane, isoflurane, enflurane, and halothane on left ventricular diastolic performance in dogs. *J Cardiothorac Vasc Anesth* 8: 618–624, 1994.
37. **Zhou YQ, Davidson L, Henkelman RM, Nieman BJ, Foster FS, Yu LX, and Chen XJ.** Ultrasound-guided left ventricular catheterization: a novel method of whole mouse perfusion for microimaging. *Lab Invest* 84: 385–389, 2004.
38. **Zhou YQ, Foster FS, Nieman BJ, Davidson L, Chen XJ, and Henkelman RM.** Comprehensive transthoracic cardiac imaging in mice using ultrasound biomicroscopy with anatomical confirmation by magnetic resonance imaging. *Physiol Genomics* 18: 232–244, 2004.
39. **Zhou YQ, Foster FS, Parkes R, and Adamson SL.** Developmental changes in left and right ventricular diastolic filling patterns in mice. *Am J Physiol Heart Circ Physiol* 285: H1563–H1575, 2003.
40. **Zhou YQ, Foster FS, Qu DW, Zhang M, Harasiewicz KA, and Adamson SL.** Applications for multifrequency ultrasound biomicroscopy in mice from implantation to adulthood. *Physiol Genomics* 10: 113–126, 2002.
41. **Zuurbier CJ, Emons VM, and Ince C.** Hemodynamics of anesthetized ventilated mouse models: aspects of anesthetics, fluid support, and strain. *Am J Physiol Heart Circ Physiol* 282: H2099–H2105, 2002.